ANALYSIS OF THE DISTRIBUTION OF PITCH ANGLES IN MODEL GALACTIC DISKS: NUMERICAL METHODS AND ALGORITHMS

WILLIAM S. RUSSELL
Columbia University and NASA Goddard Institute for Space Studies, 2880 Broadway, New York, NY 10025-7819

AND

WILLIAM W. ROBERTS, JR.
Department of Applied Mathematics and Virginia Institute for Theoretical Astronomy,
Olsson Hall, University of Virginia, Charlottesville, VA 22903-2442
Received 1992 April 23; accepted 1993 March 9

ABSTRACT

Numerical methods and algorithms are developed for analyzing the morphology of global and local structure in prototype and observed disk-shaped galaxies. One prototype spiral galaxy, taken from the 1992 theoretical-computational studies of Roberts et al., serves as the representative candidate to be analyzed in this paper. From the computed distribution of the gaseous component, "partitioning" methods based on nearest-neighbor and Voronoi polyhedra calculations are applied to capture regions of high-population gas density associated with local arm segments, spurs, feathers, and secondary features. The pitch angle and length of each of these features are determined using least-squares procedures minimizing perpendicular distances from data points to the regression curve in adapted logarithmic spiral coordinates. The resulting least-squares approximations are further checked for goodness of fit using the Kolmogorov-Smirnov test. Despite the fact that the representative prototype model galaxy is driven by an underlying global two-armed density wave of 10°–15° pitch angle, the gas response is found to exhibit many local and mesoscale spiral features of much greater pitch angle. These features are attributed to the self-gravitational effects of the gas itself on local scales. Prominent peaks are found in the computed pitch angle distribution between 20° and 40°; these are attributed to spurs and local arm segments that branch off the underlying 10°–15° modal density-wave-driven global spiral pattern. Prominent highly inclined spurs and feathers in the outer half of the prototype galaxy are found to give rise to a peak pitch angle distribution between 50° and 55°.

Subject headings: galaxies: ISM — galaxies: kinematics and dynamics — galaxies: spiral

1. INTRODUCTION

Explanation of the spiral structure manifested in many disk-shaped galaxies has been a challenge to astronomers and astrophysicists for over a century. It has been observed that global spiral arms are actually composed of successive local spiral features (secondary features), but thorough examination of these subsections or isolated segments has never been undertaken through quantitative methods. The work presented here isolates and investigates the morphological characteristics of this spiral structure on global and local scales in prototype galaxies.

In the past, little attention has been paid to properties such as length and pitch angle (the angle between the feature and the tangent of a circle at the same radius as the starting point of the feature). Lynds (1970) made studies of the dust lane widths and dark feathers that occurred in Sc-type galaxies. More recently, Elmegreen (1979, 1980) made approximate measurements of primary spurs appearing in a variety of spiral galaxies. The lengths, widths, and pitch angles of 28 primary spurs were measured. The estimated error in pitch angle calculations was ±5° since uncertainties arose in defining precisely the edges of features. This imprecision also lead to errors of the order 0.1 kpc in length and width approximations. Error bounds such as these were to be expected and have motivated the following questions: What constitutes a feature? How exactly are edges of features defined? Is there an optimal pitch angle and length for a given feature?

Mathematical-computational simulations carried out by Roberts et al. (1992; see also Roberts, Lowe, & Adler 1990; Roberts 1992a, b, 1993) follow the dynamics of approximately 10,000 gas clouds. These clouds undergo collisions, participate in star formation, interact through their own self-gravitation, and in several cases are driven by a modal spiral density wave (SDW) pattern (Bertin et al. 1989a, b; Lowe 1988; also see Lin & Shu 1964, 1966).

Earlier model simulations by Levinson & Roberts (1981), Roberts & Hausman (1984), Hausman & Roberts (1984), and Roberts & Stewart (1987) considered non–self-gravitating gas and used only approximate SDW modes. They mimicked the stochastic, self-propagating star formation process (SSPSF) mechanism (Mueller & Arnett 1976; Gerola & Seiden 1979, and Seiden & Gerola 1979) by allowing young stellar associations to form at the sites of cloud collisions; supernovae explode within these young stellar associations after some stochastic delay time. These supernovae events can subsequently cause other young stellar associations to be created in neighboring clouds. The self-gravity force field effects, created by the gravitational pull of other gas clouds in the interstellar medium, was modeled by Adler (1989). Using Fourier transform techniques adapted from those developed by Miller (1976, 1978), Miller & Smith (1979a, b), and Smith & Miller (1986), Adler was able to effectively model the gravitational influence of the cloud ensemble. It is the gaseous self-gravity that is instrumental in creating strong density inhomogeneities

along spiral arms and in forming various types of interesting secondary spiral features (Roberts & Adler 1989).

Each gas cloud in the computer simulations essentially represents a giant molecular cloud (GMC) compatible with approximately 10^7 solar masses. These GMCs (or simple clouds) can be thought of as partly molecular, partly atomic clouds consequently spanning the entire spectrum of cloudy interstellar matter. The clouds are of uniform size and shape and thus merely building blocks in the spiral galactic structure. However, important physical properties can be ascertained, and through animation techniques, physical phenomena observed.

The prototype galaxy of primary focus analyzed in this paper constitutes one representative model galaxy taken from the multi-parameter space, theoretical-computational studies of Roberts et al. (1992). The gaseous component in this case is made up of a low-dispersion-speed system of gas clouds (e.g., with a one-dimensional dispersion speed of 6 km s^{-1}) that constitute approximately 6% of the total galactic mass and whose average disk mass surface density, for example, at an annular radius of the 10 kpc neighborhood, constitutes approximately 20% of the total galactic mass surface density. The dynamics of the gas cloud system is governed in part by the self-gravitational forces that act between constituent clouds, together with the spiral perturbed gravitational field of a computed density wave mode that approximates a $10°$–$15°$ spiral in the outer parts of the disk. Energy-dissipating cloud-cloud collisions together with energy-replenishing star formation activity (culminating in supernovae explosions with velocity boosts to neighboring gas clouds) also govern the dynamics of the gas cloud system on local scales.

In contrast to "ruler-and-compass" or "hand-to-eye" measurements employed by previous investigators, an *automated mathematical method* is formulated to (1) capture distinct features evolving within the spiral galactic disk and (2) measure their lengths and pitch angles. Carlberg & Freedman (1985) had limited success with a logarithmic spiral decomposition method used to describe the morphology of global arms arising in model galaxies dominated solely by gravity and dissipation. However, this method is unsuitable for examining characteristics of local features (see Russell 1991).

To isolate the prominent features, methods are employed which are based on the premise that regions of high cloud concentration constitute features. Hence, if gas clouds contributing to a dense region can be ascertained, then the associated feature has effectively been isolated. The first algorithm selects only clouds which have a sufficient number of neighbors within a certain distance tolerance to contribute to a feature. The second algorithm utilizes the Voronoi diagram (Voronoi 1908) where each cloud is assumed to own a certain area of the galaxy. Obviously, clouds in dense regions are assigned smaller areas, and consequently clouds associated with small Voronoi polyhedra are selected as contributing to a feature. These two "partitioning" methods are described in § 2.

Once the features have been captured, the method of least squares is incorporated into the mathematical method to approximate the preferred orientations. Since the features, from long, trailing global arms to short spurs, have a spiral form (generally due to differential rotation of the galaxy), it is appropriate to perform the least-squares analysis in a spiral coordinate system. The logarithmic spiral (log-spiral) $r = r_0 e^{\theta/p}$ has the attractive property of constant pitch angle. Hence, the spiral coordinates $(\ln r, \theta)$ are employed. The least-squares algorithm is described in § 3.

The synergism of the partitioning algorithms and the modified least-squares procedure is examined on a test galaxy whose spiral properties are already known (see Appendix). Section 4 assesses the accuracy and effectiveness of the method to the prototype galaxy of Roberts et al. (1990, 1992). Conclusions for this prototype galactic system are drawn concerning the distributions of pitch angles and subsequently related to the different morphologies of the galaxies.

2. THE PARTITIONING ALGORITHMS

To isolate the distinct features in the spiral galactic disk, a mathematical model must be developed. Initially, the gas cloud distribution is separated into areas of high density which constitute secondary features. This process is termed *clumping*; two algorithms for generating these clumps will be described. The precision of the partitioning algorithms is of utmost importance to the overall success of the mathematical method. Each cloud can contribute to one feature only. It is essential that all clouds constituting a single feature are isolated and thus not included in any other feature. The pitch angle of a feature may change significantly if clouds are missed or accidentally included.

Automated partitioning algorithms are formulated so that any spiral galactic disk simulation (at any epoch) of the type done by Roberts et al. (1992) can be separated into feathers, spurs, bridges, and other secondary features in order to further compute the distribution of pitch angles of these spiral inhomogeneities.

2.1. *The Distance Tolerance Algorithm*

Clouds in regions of high density necessarily have closer neighboring clouds than those in sparse regions. This provides the foundation of the distance tolerance (d_{tol}) algorithm. Clouds are assumed to contribute to features if and only if they have a sufficient number of neighboring clouds within a given distance tolerance. After eliminating clouds not satisfying this criterion, the remaining clouds are sorted into clumps. Each cloud, along with its neighbors, is assigned an initial clump number or *tag*. If two initially separate clumps have any common clouds, then the clumps are joined. Following this procedure for every cloud ensures that each distinct cloud will contribute to only one clump. The resulting clumps are treated as individual features.

Several refinements need to be made before this method can be successfully implemented. The foremost problem is due to the number of clouds N ($= 10,000$) distributed over the prototype galactic disk. Since the method compares distances between clouds there are, intuitively, $O(N^2)$ comparisons, which is computationally unacceptable. The problem is overcome by using a *small cell/big cell* technique. A Cartesian grid is generated over the galactic disk. For each cloud within each *small cell* (of the Cartesian grid), the distance between it and every other cloud in that small cell is found. Consequently, only distances between a cloud and other clouds in the same small cell (instead of every cloud in the galaxy) are computed. If a cloud lies in the corner of a cell it may have additional neighboring clouds within d_{tol} lying in an adjacent cell. This may cause the cloud to be omitted since it may not have a sufficient number of neighboring clouds in its small cell within d_{tol}. By introducing a *big cell* formed by the nine adjacent cells centered about the associated small cell, the problem of cloud omission is overcome. For each cloud C_i in the small cell, distances are found between C_i and every cloud in its associated big cell. If there are M small cells this is roughly a $9N^2/M$

algorithm; for the overlaid computational grid, this results in a significant reduction in execution time.

Another problem related to the choice of a d_{tol} value or expression also arises. Initially, a constant value was used for program testing, but this selection was fairly arbitrary. This constant d_{tol} seemed to produce large clumps toward the center of the galactic disk and small clumps at the outer edges. Consequently, this choice of d_{tol} condensed several features as a single clump in internal regions of the galactic disk, but split distinct features into small clumps at outer radial values. This was a direct result of a decrease in cloud density with increased radial distance; features located closer to the outer edge of the galactic disk are generally less dense than those toward the center. Therefore, to successfully capture all the features, an expression for d_{tol} which is a monotonically increasing function of galactic radius must be derived.

For the prototype galaxy to which this analysis is to be applied, the phase of the spiral perturbation representing a spiral density wave mode is not far from a constant log-spiral of the form

$$\Phi(r) = \frac{m \ln (r/r_0)}{\tan (i_0)} , \qquad (1)$$

where the pitch angle i_0 satisfies $\tan (i_0) = r^{-1} dr/d\theta$ where θ increases counterclockwise. The wave number vector $\mathbf{k}$ of the general wave form $e^{im\mathbf{k} \cdot \mathbf{r}}$, where $\mathbf{r}$ is a position vector, can be split into radial and axial components k_r and k_θ, respectively:

$$k_r = \frac{\partial \Phi}{\partial r} = \frac{m}{r \tan (i_0)} , \qquad (2a)$$

$$k_\theta = \frac{1}{r} \frac{\partial \Phi}{\partial \theta} = \frac{1}{r} \frac{\partial \Phi}{\partial r} \frac{dr}{d\theta} = \frac{m}{r} . \qquad (2b)$$

It therefore follows that

$$\mathbf{k} \cdot \mathbf{k} = k^2 = k_r^2 + k_\theta^2 = \frac{m^2}{r^2 \sin^2 (i_0)} , \qquad (3)$$

but since the pitch angle parameter $p = \tan (i_0)$ implies that $\sin (i_0) = p/(1 + p^2)^{1/2}$, it follows that

$$k = \frac{m(1 + p^2)^{1/2}}{rp} . \qquad (4)$$

Hence the wavelength λ satisfies

$$\lambda = \frac{2\pi}{k} = \frac{2\pi rp}{m(1 + p^2)^{1/2}} , \qquad (5)$$

implying that wavelength varies linearly as a function of radius. More simply, the distance between spiral arms grows linearly with r. It is conjectured that the expected distances between clouds therefore also grows linearly with r. More formally:

$$d_{tol} = \zeta r , \qquad (6)$$

where ζ is a constant. An initial choice of $\zeta = 0.02$ captures the features throughout the galactic disk very well.

2.2. The Area Tolerance Algorithm

To determine the accuracy of the d_{tol} algorithm, it was necessary to develop another quite different clumping algorithm.

This algorithm, henceforth referred to as the a_{tol} algorithm, is based on the idea that every cloud "owns" a certain portion of space in the shape of a polyhedron. This portion of space is the area surrounding each cloud C_i, closer to C_i than any neighboring cloud C_j and referred to here as the Voronoi polyhedron. The set of Voronoi polyhedra of an associated distribution of a finite set of points S is known as the Voronoi diagram.

The Voronoi diagram of S is a well-known structure which makes available precise information concerning S. It has had numerous applications in a broad spectrum of the natural and physical sciences including physics (Brostow, Dussault, & Fox 1978), biology (Blum 1973), and geography (Rhynsburger 1972, 1973), and since allotting spaces to molecules can be accomplished by this technique, it is also used in molecular physics, biochemistry, materials science, physical chemistry, and of course astronomy and astrophysics (Kiang 1966). Not surprisingly, these polyhedra were first defined by mathematicians (Dirichlet 1850; Voronoi 1908) and are variously known as Dirichlet regions, Thiessen polygons, Wigner-Seitz cells, or Voronoi polyhedra; this latter description is the terminology used here.

Given a configuration of points $C_1, C_2, ..., C_N$ in L-dimensional Euclidean space E, the Voronoi polyhedron V_i around a given center C_i is the set of points, or area in E closer to C_i than to any C_j: more formally

$$V_i = \{x \in E: d(x, C_i) \le d(x, C_j), j = 1, ..., n\} , \qquad (7)$$

where d denotes distance. The polyhedra are intersections of half spaces and are always convex. The polyhedra partition in a unique way, and the resulting diagram is known as the Voronoi diagram.

The Voronoi polyhedron V_i for a cloud C_i is defined as the interior polygon constructed by the perpendicular bisectors of C_i and all other clouds C_j. A neighbor is defined as a cloud C_j whose perpendicular bisector contributes to V_i, that is, an edge of V_i. The Voronoi diagram formed from the distribution of clouds in the galaxy will produce small area polyhedra for clouds in dense regions and large area polyhedra for clouds in sparse regions. The idea behind determining the Voronoi diagram is to calculate the areas of each of the polyhedra and throw away all clouds with associated area greater than some tolerance area a_{tol}. From the remaining distribution, each cloud is tagged with a clump number along with all its remaining neighbors. Then each of the neighbor's neighbors is tagged with the same clump number. This procedure continues until every cloud has been tagged. As in the previous algorithm, if any cloud is common to two or more clumps, these clumps will be joined to ensure that each cloud will contribute to a unique clump.

There are many procedures for constructing Voronoi polyhedra. Unfortunately, the simplest methods are so often the most computationally inefficient. The method used here is that developed by Brostow et al. (1978): more details on its implementation are described in Russell (1991).

First, the neighbors of C_i are categorized. There are four classes of neighbors: (1) direct neighbors (the midpoint of the line $C_i C_j$ lies on the polyhedron) (2) indirect neighbors (the perpendicular bisector of $C_i C_j$ contributes to V_i, but the midpoint of $C_i C_j$ lies outside V_i), (3) degenerate neighbors (the midpoint of $C_i C_j$ is just a vertex of V_i), and (4) quasi-direct neighbors (C_j is a direct neighbor in the absence of all indirect neighbors).

The quasi-direct neighbors generate a direct polyhedron D, and the quasi-direct, along with the indirect neighbors, generate V. On the average, direct polyhedra D have simpler shapes, or fewer faces, than Voronoi polyhedra V. Hence, the idea is first to construct the polyhedra D and then proceed toward V.

The overall work involved in finding the direct neighbors is $O(N^2 \ln N)$. Obviously for $N = 10,000$ clouds this is unacceptable. Consequently, the *small cell/big cell* approach is also adopted here. The sorting algorithm "quicksort" then becomes $O[(9N/M)\ln(9N/M)]$, where M is the number of cells in the computational grid. Although this is done N times to make the overall work roughly $O[(9N^2/M)\ln(9N/M)]$, this modification allows the method to be computationally viable.

Calculation of the indirect neighbors of cloud C_i is achieved by first circumscribing a sphere of diameter d_i around D_i, the direct polyhedron. Then, any point more than d_i away from C_i cannot be a neighbor; d_i is by definition twice the distance from C_i to the furthest vertex of D_i. This eliminates many, if not most, of the points as indirect neighbors. Those which remain are used to find V_i from D_i. Vertices, and sometimes edges, are cut off by edges generated by indirect neighbors. Once the set of C_j, the possible indirect neighbors of V_i, has been exhausted, the Voronoi polyhedron V_i, by definition, is left. Figure 1 shows a plot of 100 randomly distributed points over a unit square along with their associated Voronoi polyhedra. Notice that the points on the outer edge have unbounded Voronoi polyhedra. Once the n vertices with coordinates (x_k^i, y_k^i), $k = 0, \ldots, n - 1$ of V_i are determined, the area of the n-sided polygon can be calculated using

$$A_i = \frac{1}{2} \left| \sum_{k=0}^{n-1} x_k^i(y_{k+1}^i - y_{k-1}^i) \right|, \tag{8}$$
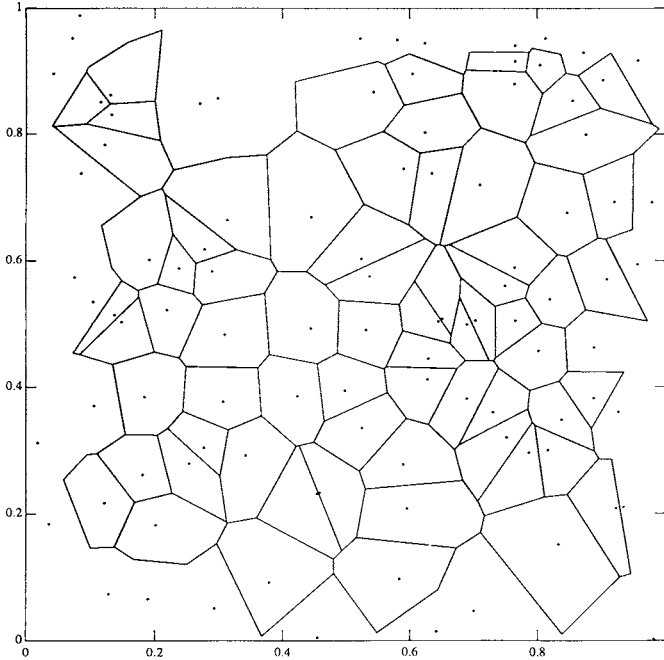
where indices are taken modulo n.

FIG. 1.—Example Voronoi Diagram. The area surrounding each particle C_i closer to C_i than any neighbor C_j is defined as the Voronoi cell V_i. For the randomly distributed particles plotted here, the neighboring particles contributing to each of C_i's Voronoi polyhedron V_i are determined, and the corresponding perpendicular bisectors are calculated.

The *small cell/big cell* approach may cause some of the neighbors of C_i to be omitted and hence, the calculation of V_i to be slightly off. While there has been no evidence of this, it should be noted that if a possible neighbor has been left out, then it must lie at a great distance from C_i (due to the width of the cells). While the calculated area of V_i for this possible case would cause V_i to be slightly larger than it would otherwise be, it will in all probability be eliminated further along in the calculation due to its large size anyway. Thus, the *small cell/big cell* approach, as well as being far more efficient, should not affect the overall calculation after the clouds with associated areas greater than a_{tol} have been eliminated.

In the same manner that a value or expression for d_{tol} was chosen, an expression for a_{tol}, the tolerance level at which areas of the Voronoi polyhedra are thrown away, must also be chosen. Since the wavelength increases linearly with r, and d_{tol} was chosen as a linear function of r, it is concluded that the natural extension for a_{tol} is a function of r^2: in particular, the following is employed:

$$a_{tol} = \pi \left(\frac{\zeta r}{2} \right)^2. \tag{9}$$

Note that $\zeta r/2$ represents half the expected distance between clouds; thus a_{tol} represents a good approximation to the area surrounding the cloud.

The final part of this algorithm involves clumping the clouds into their corresponding features. This method is quite similar in nature to that employed in the previous section. If the Voronoi polyhedron V_i of cloud C_i has area less than a_{tol}, then the cloud number and position, plus the cloud numbers of the indirect and quasi-direct neighbors of C_i, are saved. Taking the clouds one at a time, C_i and its neighbors C_k are tagged with a clump number. If any of these clouds have already been tagged (i.e., already assigned a clump number), then the clumps are combined. This process continues until all the clouds have been assigned to a feature.

3. THE LEAST-SQUARES ALGORITHMS

For two random variables x and y, the standard least-squares method calculates the parameters of the equation for a straight line which give a best fit to the set (x_i, y_i). These parameters for the standard least-squares method minimize the error function Q_y, the sum of the squares of the vertical deviations. For simplicity, suppose that a distribution of $\mathcal{N}$ points (x_i, y_i) in Cartesian coordinates is to be analyzed.

3.1. *Standard Least Squares*

The pitch angle must somehow be approximated, given the (x_i, y_i) coordinates of each of the clouds contributing to each feature. For short features, a good approximation to the slope can be obtained using a linear least-squares fit to the form

$$\hat{y} = \hat{\alpha} + \hat{\beta}x, \tag{10}$$

called the estimated regression line. The problem is to obtain estimates $\hat{\alpha}$ and $\hat{\beta}$ such that $\hat{y}$ provides the best possible fit to the given data: $\hat{\alpha}$ and $\hat{\beta}$ are defined as the values for which the error function

$$Q_y = \sum_{i=1}^{\mathcal{N}} (e_y)_i^2 = \sum_{i=1}^{\mathcal{N}} [y_i - (\hat{\alpha} + \hat{\beta}x_i)]^2 \tag{11}$$

is a minimum. Differentiating partially with respect to $\hat{\alpha}$ and $\hat{\beta}$, and equating these partial derivatives to zero yields the system

of normal equations. The least-squares estimate of $\hat{\beta}$ becomes

$$\hat{\beta} = \frac{\mathcal{N}(\sum_{i=1}^{\mathcal{N}} x_i y_i) - (\sum_{i=1}^{\mathcal{N}} x_i)(\sum_{i=1}^{\mathcal{N}} y_i)}{\mathcal{N}(\sum_{i=1}^{\mathcal{N}} x_i^2) - (\sum_{i=1}^{\mathcal{N}} x_i)^2} , \tag{12}$$

and hence $\hat{\alpha}$ becomes

$$\hat{\alpha} = \frac{\sum_{i=1}^{\mathcal{N}} y_i - \hat{\beta} \sum_{i=1}^{\mathcal{N}} x_i}{\mathcal{N}} . \tag{13}$$

The interest is in the orientation of the cloud set, that is, the value of $\hat{\beta}$.

For some cloud distributions, the least-squares approximation previously described is highly inaccurate. For example, if a distribution of points had a "north-south" orientation, vertical deviations from any point to the vertical regression lines would effectively be infinite. Hence, any method of trying to minimize vertical deviations would lead to a misleading regression line. One way around this is also to minimize the horizontal deviations and find the estimates $\hat{\gamma}$ and $\hat{\delta}$ such that the estimated regression line

$$\hat{x} = \hat{\gamma} + \hat{\delta} y \tag{14}$$

provides the best possible fit to the data. Obviously, the least-squares estimates of the regression coefficients are the values $\hat{\gamma}$ and $\hat{\delta}$ for which the quantity

$$Q_x = \sum_{i=1}^{\mathcal{N}} (e_x)_i^2 = \sum_{i=1}^{\mathcal{N}} [x_i - (\hat{\gamma} + \hat{\delta} y_i)]^2 \tag{15}$$

is a minimum. By a similar argument

$$\hat{\delta} = \frac{\mathcal{N}(\sum_{i=1}^{\mathcal{N}} x_i y_i) - (\sum_{i=1}^{\mathcal{N}} x_i)(\sum_{i=1}^{\mathcal{N}} y_i)}{\mathcal{N}(\sum_{i=1}^{\mathcal{N}} y_i^2) - (\sum_{i=1}^{\mathcal{N}} y_i)^2} \tag{16}$$

and

$$\hat{\gamma} = \frac{\sum_{i=1}^{\mathcal{N}} x_i - \hat{\delta} \sum_{i=1}^{\mathcal{N}} y_i}{\mathcal{N}} . \tag{17}$$

Returning to the expression for Q_x the value of the error can be calculated from the values of $\hat{\gamma}$ and $\hat{\delta}$ in equations (16) and (17). By the same means, Q_y can be found by substituting equations (12) and (13) into equation (11).

3.2. Modified Least Squares

A best-fit line will vary depending on the coordinate system used. For instance, if another coordinate system (ξ, η) were to be used, the resulting slope would be different from those found previously.

There is clearly one distinct best-fit curve which minimizes the various error functions Q and is associated with a specific coordinate system. This is defined here as the superior fit and is the line $ax + by + c = 0$ which minimizes the sum of the squares of the shortest distances (perpendicular distances) from all points (x_i, y_i) to the line. It follows that the coordinate system which gives this best fit is (ξ, η) where either the ξ or η direction is also the direction in which the distances from the points to the least-squares line are minimized, that is, the slope of this least-squares line is parallel to either ξ or η. For the superior fit calculation, in order to minimize the sum of the perpendicular distances from each point to the line $y = \hat{\alpha} + \hat{\beta}x$, a more complicated function than that given in equation (11) must be minimized. Also, it is beneficial to consider the least-

squares line

$$ax + by + c = 0 \tag{18}$$

(in Cartesian coordinates) to eliminate any possibility of singularities.

Since the perpendicular distance from a point (x_i, y_i) to a line $ax + by + c = 0$ is given by

$$\frac{|ax_i + by_i + c|}{(a^2 + b^2)^{1/2}} , \tag{19}$$

it follows that

$$Q_s = \sum_{i=1}^{\mathcal{N}} e_{s_i}^2 = \sum_{i=1}^{\mathcal{N}} \frac{(ax_i + by_i + c)^2}{a^2 + b^2} \tag{20}$$

must be minimized. Differentiating partially with respect to a, b, and c and equating to zero gives the new set of equations which has to be solved for the new regression estimates a, b, and c. Assuming that cov $(x, y) \neq 0$ the following equality is obtained:

$$\frac{a^2}{b^2} + 2T \frac{a}{b} - 1 = 0 , \tag{21}$$

where

$$T = \frac{1}{2} \left[\frac{\mathcal{N} \sum_{i=1}^{\mathcal{N}} x_i^2 - (\sum_{i=1}^{\mathcal{N}} x_i)^2 - \mathcal{N} \sum_{i=1}^{\mathcal{N}} y_i^2 + (\sum_{i=1}^{\mathcal{N}} y_i)^2}{\sum_{i=1}^{\mathcal{N}} x_i \sum_{i=1}^{\mathcal{N}} y_i - \mathcal{N} \sum_{i=1}^{\mathcal{N}} x_i y_i} \right] . \tag{22}$$

Hence the solutions to equation (4) are

$$\frac{a}{b} = -T \pm (T^2 + 1)^{1/2} \tag{23}$$

and hence

$$\frac{c}{b} = -\frac{a}{b} \frac{1}{\mathcal{N}} \sum_{i=1}^{\mathcal{N}} x_i - \frac{1}{\mathcal{N}} \sum_{i=1}^{\mathcal{N}} y_i , \tag{24}$$

which gives a regression line $y = -(a/b)x - c/b$.

Notice that if a or b is zero then cov (x, y) is zero, and from equations (12) and (16) $\hat{\beta}$ is zero or $\hat{\delta}^{-1}$ is infinite. Moreover, since these represent the slopes of the regression lines minimizing the vertical and horizontal deviations, respectively, which are exactly the perpendicular distances, it follows that the superior fit must be either the line

$$y = -\frac{c}{b} = \frac{1}{\mathcal{N}} \sum_{i=1}^{\mathcal{N}} y_i \quad \text{if } S_{yy} \leq S_{xx} \tag{25}$$

or the line

$$x = -\frac{c}{a} = \frac{1}{\mathcal{N}} \sum_{i=1}^{\mathcal{N}} x_i \quad \text{if } S_{yy} \geq S_{xx} \tag{26}$$

where

$$S_{xx} = \sum_{i=1}^{\mathcal{N}} x_i^2 - \frac{1}{\mathcal{N}} \left(\sum_{i=1}^{\mathcal{N}} x_i \right)^2 \quad \text{and}$$

$$S_{yy} = \sum_{i=1}^{\mathcal{N}} y_i^2 - \frac{1}{\mathcal{N}} \left(\sum_{i=1}^{\mathcal{N}} y_i \right)^2 . \tag{27}$$

For simplicity, suppose that $\tau = a/b$ and $v = c/b$. Then equation (20) can be rewritten as

$$Q_s(\tau, v) = \sum_{i=1}^{\mathcal{N}} \frac{(\tau x_i + y_i + v)^2}{\tau^2 + 1} . \tag{28}$$

It is possible to determine which root in equation (23) gives the smallest error Q_s by studying the properties of Hessian H of Q_s (τ, v) given by

$$H = \begin{bmatrix} (Q_s)_{\tau\tau} & (Q_s)_{\tau v} \\ (Q_s)_{v\tau} & (Q_s)_{vv} \end{bmatrix} . \tag{29}$$

Alternatively, instead of using $ax + by + c = 0$, the Cartesian coordinate system with origin at the center of gravity of the distribution of clouds can be used so that the regression line simply becomes $ax + by = 0$. The distance from a point (x_i, y_i) to this line is given by $|ax_i + by_i|/(a^2 + b^2)^{1/2}$, and it follows that $\sum_{i=1}^{\mathcal{N}} (ax_i + by_i)^2/(a^2 + b^2)$ must be minimized. This is equivalent to minimizing $\sum_{i=1}^{\mathcal{N}} (ax_i + by_i)^2$ under the constraint $a^2 + b^2 = 1$. By letting A and x be defined by

$$A = \begin{bmatrix} x_1 & x_2 \dots x_{\mathcal{N}} \\ y_1 & y_2 \dots y_{\mathcal{N}} \end{bmatrix}^T , \quad x = \begin{bmatrix} a \\ b \end{bmatrix} , \tag{30}$$

it follows that $\sum_{i=1}^{\mathcal{N}} (ax_i + by_i)^2 = \| Ax \|_2^2$ and $a^2 + b^2 = \| x \|_2^2$. Hence the problem is reduced to minimizing $\| Ax \|_2$ under the constraint $\| x \|_2 = 1$. The well-known solution x to this problem is the eigenvector associated with the smallest eigenvalue of $A^T A$, where

$$A^T A = \begin{bmatrix} \sum_{i=1}^{\mathcal{N}} x_i^2 & \sum_{i=1}^{\mathcal{N}} x_i y_i \\ \sum_{i=1}^{\mathcal{N}} x_i y_i & \sum_{i=1}^{\mathcal{N}} y_i^2 \end{bmatrix} . \tag{31}$$

Hence, by calculating the quantities in the matrix in equation (31), the eigenvalues λ can be found by solving $\det (A^T A - \lambda I) = 0$ and the eigenvectors by solving $(A^T A - \lambda I)x = 0$. Although expanding this determinant and solving for λ is rather cumbersome, it turns out that the ratio a/b is exactly the same as equation (23) with T given by equation (22). This particular least-squares approximation of minimizing perpendicular deviations is also referred to in the literature as the geometric mean regression line.

3.3. Extensions to a Spiral Coordinate System

It was evident that using a linear least-squares approach gave only first-approximation results. Hence a more accurate least squares-approach was developed which could cope with the curvature of the longer spurs and spiral arms, as well as the shorter secondary features.

The model galaxies on which the pitch-angle analyses are performed are generated using clouds representing gas clouds. The cloud orbits are influenced by several factors, in particular, a spiral-perturbed forcing taking the form of a density wave *modal spiral*. The global spiral structure consists of two log-spiral arms asymptotically approaching an inclination of 10°. For this reason, least-squares estimates are developed which fit log-spirals through the features. The 10° pitch angle should now be picked up for the longer arms, and pitch angles of the shorter features should be estimated more accurately.

A best-fit curve of the form

$$r = r_0 \exp \left(\frac{\theta}{p} \right) \tag{32}$$

is required, where p is the pitch-angle parameter for the feature being analyzed in the least-squares calculation and θ increases with r along a spiral arm. Taking the logarithm of both sides gives

$$\theta = \hat{\alpha} + \hat{\beta} \ln r , \tag{33}$$

where $\hat{\alpha} = -p \ln r_0$ and $\hat{\beta} = p$. Note that equation (33) can be written in dimensionless form as $\ln (r/r_0) = \theta/p$. Thus, since both θ and $\ln r$ are dimensionless, the previous analysis of finding the superior fit can be applied successfully in this *spiral coordinate system*.

Minimizing the perpendicular error in $(\ln r, \theta)$ space results in

$$Q_\perp^s = \sum_{i=1}^{\mathcal{N}} (e_\perp)_i^2 = \sum_{i=1}^{\mathcal{N}} \frac{[\theta_i - (\hat{\alpha} + \hat{\beta} \ln r_i)]^2}{1 + \hat{\beta}^2} \tag{34}$$

being minimized. Following the same analysis as in Cartesian coordinates it can be shown that

$$\hat{\beta}^2 - 2T\hat{\beta} - 1 = 0 , \tag{35}$$

where

$$T = \frac{1}{2}$$
$$\times \left[\frac{\mathcal{N} \sum_{i=1}^{\mathcal{N}} \ln r_i^2 - (\sum_{i=1}^{\mathcal{N}} \ln r_i)^2 - \mathcal{N} \sum_{i=1}^{\mathcal{N}} \theta_i^2 + (\sum_{i=1}^{\mathcal{N}} \theta_i)^2}{\sum_{i=1}^{\mathcal{N}} \ln r_i \sum_{i=1}^{\mathcal{N}} \theta_i - \mathcal{N} \sum_{i=1}^{\mathcal{N}} \ln r_i \theta_i} \right] . \tag{36}$$

Hence the solutions to equation (35) are

$$\hat{\beta} = T \pm (T^2 + 1)^{1/2} \tag{37}$$

and

$$\hat{\alpha} = -\hat{\beta} \frac{1}{\mathcal{N}} \sum_{i=1}^{\mathcal{N}} \ln r_i + \frac{1}{\mathcal{N}} \sum_{i=1}^{\mathcal{N}} \theta_i , \tag{38}$$

which give the regression coefficients in equation (23). It follows that the pitch angle $i_0 = \tan^{-1} (1/\hat{\beta})$.

The length of each of the spiral features must also be calculated. The length s of a curve is given in polar coordinates by

$$s = \int_{\theta_1}^{\theta_2} \left\{ \left[\left(\frac{dr}{d\theta} \right)^2 + r^2 \right] \right\}^{1/2} d\theta . \tag{39}$$

Since the general form of the least-squares estimate is $\theta = \hat{\alpha} + \hat{\beta} \ln r$ (where $\hat{\beta}$ is assumed nonzero), it follows that

$$s = (1 + \hat{\beta}^{-2})^{1/2} \int_{\theta_1}^{\theta_2} \exp \left[\frac{(\theta - \hat{\alpha})}{\hat{\beta}} \right] d\theta . \tag{40}$$

Given θ_1 and θ_2 the curve length can then be expressed as

$$s = K \left[\exp \left(\frac{\theta_2}{\hat{\beta}} \right) - \exp \left(\frac{\theta_1}{\hat{\beta}} \right) \right] , \tag{41}$$

where $K = (\hat{\beta}^2 + 1)^{1/2} \exp (-\hat{\alpha}/\hat{\beta})$. Note that for $\hat{\beta} = 0$, the pitch angle is $\pi/2$ and therefore a straight line (passing through the origin). This case is simple and treated separately.

3.4. The Kolmogorov-Smirnov Test

The clumping algorithms described previously are not invincible to joining two predetermined distinct features by accident

and treating the resulting distribution of clouds as a single feature. Moreover, the least-squares method will proceed to fit an inaccurate regression line through this distribution of points. This sort of inaccurate least-squares estimate may strongly affect the final pitch-angle distribution, and hence these inaccuracies must be detected and eliminated from any further analysis.

The Kolmogorov-Smirnov test represents a formal procedure for checking whether results from least-squares analyses do in fact agree with the underlying probabilistic model assumed for the original data. The assumption with the least-squares calculation is that once the least-squares estimates have been found, the distribution of errors (which in this case are the minimum distances from the data points to the least-squares regression line) are normally distributed with mean zero.

Suppose Y is a continuous random variable having distribution function $F(y)$. A random sample of n realizations of Y yields the observations $y_1, \ldots, y_n$. Reordering these observed values from smallest to largest, and denoting the ordered y_i by $y_{(1)} \leq y_{(2)} \leq \cdots \leq y_{(n)}$, the empirical distribution function can be expressed (assuming $y_0 = -\infty$) as

$F_n(y) = $ fraction of the sample less than or equal to y

$$= \begin{cases} \dfrac{(i-1)}{n} & \text{if} \quad y_{(i-1)} \leq y \leq y_{(i)} \quad i = 1, \ldots, n \\ 1 & \text{if} \quad y \geq y_{(n)} \end{cases} \quad (42)$$

The null hypothesis that the continuous random variable Y (error value for the analysis here) is assumed to have a distribution function given by $F(y)$ (normal distribution with mean μ and standard deviation σ) is rejected if the K-S statistic D, based upon the maximum distance between $F(y)$ and $F_n(y)$, and defined by

$$D = \max_y |F(y) - F_n(y)| , \quad (43)$$

is too large. To find the observed value of D, it is necessary to check only

$$D^+ = \max_{1 \leq i \leq n} \left[\frac{i}{n} - F(y_i) \right] \quad \text{and} \quad D^- = \max_{1 \leq i \leq n} \left[F(y_i) - \frac{i-1}{n} \right] \quad (44)$$

and define $D = \max(D^+, D^-)$. For a normal $F(y)$ with an unknown mean and variance, the modified form of D is given by

$$D_{\text{mod}} = D(n^{1/2} - 0.01 + 0.85/n^{1/2}) , \quad (45)$$

and the value of this modified D cutting off an upper-tail area of 0.01 is 1.035 (Stephens 1974).

The K-S test is performed in both $(\ln r, \theta)$ space and (x, y) space. The errors in $(\ln r, \theta)$ space are defined as

$$E_i^s = \frac{\theta_i - (\hat{\alpha} + \hat{\beta} \ln r_i)}{(1 + \hat{\beta}^2)^{1/2}} . \quad (46)$$

Since the exact value of the shortest distance from a point to a spiral is difficult to calculate, the following approximation in the (x, y) space is used:

$$E_i^c = \frac{d_r \, d_\theta}{(d_r^2 + d_\theta^2)^{1/2}} , \quad (47)$$

where

$$d_r = r_i - \exp\left[(\theta_i - \hat{\alpha})/\hat{\beta}\right] , \quad (48a)$$

$$d_\theta = r_i |\theta_i - (\hat{\alpha} + \hat{\beta} \ln r_i)| . \quad (48b)$$

For each of the distributions of errors E_i^s and E_i^c, the mean and standard deviation are calculated. Since a normal distribution of mean μ^s and standard deviation σ^s is assumed, the probability that Y is less than or equal to y is given by

$$\Pr\{Y \leq y\} = P\left(\frac{y - \mu^s}{\sigma^s}\right) \quad (49)$$

where

$$P(x) = \frac{1}{(2\pi)^{1/2}} \int_{-\infty}^{x} e^{-s^2/2} \, ds . \quad (50)$$

The following approximation for $P(x)$ is taken from Abramowitz & Stegun (1972):

$$P(x) = 1 - Z(x)(b_1 t + b_2 t^2 + b_3 t^3 + b_4 t^4 + b_5 t^5) + \epsilon(x) , \quad (51)$$

where

$$t = (1 + 0.2316419x)^{-1} ; \quad |\epsilon(x)| < 7.5 \times 10^{-8} , \quad (52)$$

$$Z(x) = \frac{1}{(2\pi)^{1/2}} e^{-x^2/2} , \quad (53)$$

with the coefficients

$$b_1 = 0.319381530, \quad b_2 = -0.356563782,$$
$$b_3 = 1.781477937, \quad b_4 = -1.821255978, \quad (54)$$
$$b_5 = 1.330274429 .$$

Hence, for each of the values of E_i^s, the probability of an error being smaller than E_i^s is calculated. This is compared with i/n and $(i - 1)/n$. The maximum value over all n values is determined and is, by definition, the K-S statistic D.

The test is applied to both sets of errors E_i^s and E_i^c. If, for both of the distributions of errors, the modified form of the K-S statistic is greater than the 0.01 tolerance level of 1.035, the least-squares estimate of the pitch angle is eliminated. This is a stricter test than simply applying the analysis to say E_i^s, that is, greater than 99% certainty that those least-squares fits eliminated using the K-S test are not accurate approximations to the orientation of the cloud distribution.

4. RESULTS AND DISCUSSION

In existing mathematical-computational simulations by Roberts et al. (1990, 1992), interstellar clouds orbit the galactic disk under the influence of a variety of forces. The cloud trajectories are orbits in the galaxy's gravitational field, perturbed by energy-dissipative cloud-cloud collisions and by velocity altering interactions with expanding supernova remnants. The force field due to self-gravity, the gravitational force induced by the neighboring clouds, is also included. It was evident that the gas mass fraction c_f of the total gas mass to total stellar mass was of paramount importance in aiding the formation and assembling of massive aggregations of clouds into giant cloud complexes, spurs, and featherlike features (Roberts &

Adler 1989). Furthermore, the fraction A_f of perturbed spiral forcing versus axisymmetric forcing played a key role in describing the global spiral structure.

The model galaxy considered here (Case 15 of Roberts et al. 1992) shown in Figure 2 combines the two parameters c_f and A_f. The strong spiral arms can be easily traced, but more striking is the abundance of secondary structure. The characteristic nature of this flocculent spiral structure is of great interest, in particular, the pitch-angle distribution and the constitution of the many secondary features. When strong spiral forcing is combined with a significant gas mass fraction, both the global spiral structure and local instabilities are present. The global spiral arms are highly disjointed and due directly to the high ratio of gas-to-stellar mass. The segments of the global arms have been oriented outward. In fact, the global arms seem to consist of a sequence of spiral density inhomogeneities each with greater orientation than the global arms. This phenomenon is more evident at inner regions of the global arms, where compact features lie closer together. The secondary features discussed here are synonymous with what many astrophysicists classify as "large cloud complexes, giant molecular clouds or superclouds" (Elmegreen 1991a, b).

It is difficult to distinguish by simple observation which are the prominent features in our model spiral galaxy and in particular which clouds truly contribute to a given feature. For this reason a set of tolerance levels is introduced. This is invoked by introducing a sequence of parameters ζ in equations (6) and (9) used in the d_{tol} and a_{tol} algorithms. A prominent feature should be captured using a majority of the tolerance values. The distribution of clouds constituting this feature will differ slightly for the sequence of ζ, but the resulting pitch angles should vary over only a few degrees at most. Hence, they will significantly contribute to the probability density function about the mean value of these resulting pitch

angles. This approach seems befitting since from observations one would be hard pressed to attach an exact pitch-angle value to any given feature: rather, one would make a measurement and claim accuracy to within a few degrees.

Nine values of ζ, for both the d_{tol} and a_{tol} clumping algorithms, are used. The values of d_{tol} are given by

$$d_{tol} = \left[0.012 + \frac{(l-1)}{500} \right] r \quad l = 1, \ldots, 9 \qquad (55)$$

and equivalently for a_{tol} by

$$a_{tol} = \frac{1}{4} \pi \left\{ \left[0.012 + \frac{(l-1)}{500} \right] r \right\}^2 \quad l = 1, \ldots, 9 . \qquad (56)$$

The spiral loci generated after application of the d_{tol} algorithm to the gas cloud distribution are presented in Figure 3. Those regression spirals which seem to do a poor job of approximating the orientation of a certain feature are eliminated by the Kolmogorov-Smirnov goodness-of-fit test, and consequently not included in the plots. Ignoring for the moment the morphology of the galactic disk, it is clear that the denser regions constituting secondary features have been successfully isolated. Furthermore, the least-squares algorithm has accurately modeled their orientations.

The method by which the distribution of pitch angles is determined is also approximate. For each integer value of i_0, pitch angles between $i_0 \pm 2°5$ for all values of ζ are summed and converted to fractions to produce the associated probability density functions. Negative pitch angles are disregarded as are those greater than $90°$. Note that the pitch-angle values computed cannot be treated as exact, but merely good approximations. Hence, this binning and averaging technique, although effectively smoothing the probability density function, is believed to furnish more appropriate information.
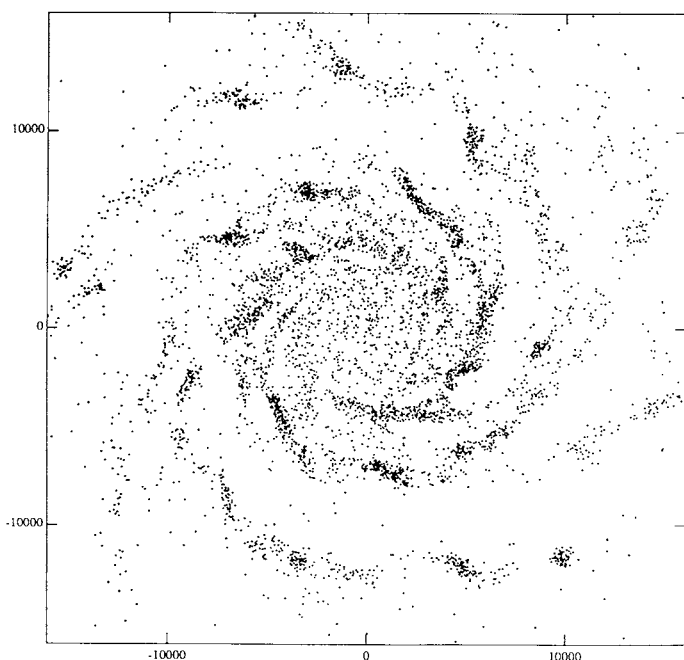

FIG. 2.—Model galaxy Case 15 at 480 Myr (taken from computational work of Roberts et al. 1992). This galaxy was simulated using strong spiral forcing (10%–15%) and a fairly high gas mass fraction ($\sim$6%). The global spiral arms are clearly disjointed and consist of a succession of distinct secondary features.
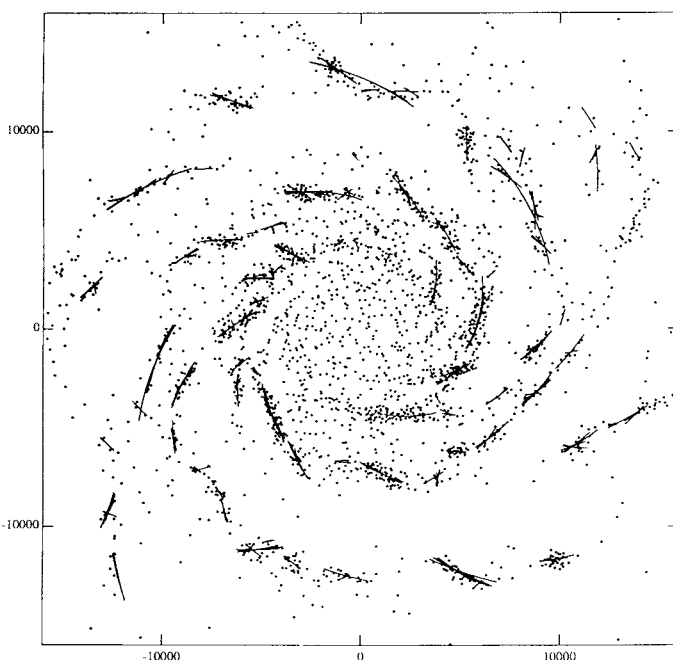

FIG. 3.—Spiral loci for model galaxy Case 15 (Roberts et al. 1992) after employing the d_{tol} partitioning algorithm and the superior fit spiral least-squares method. Each spiral loci represents how the d_{tol} algorithm has captured a feature. For each of the features captured the orientation has been successfully modeled.

The probability density functions associated with the spiral loci presented in Figure 3 are displayed in Figure 4. By applying weights which are proportional to a feature's length, the pitch angles of longer features become more prominent (Fig. 4b). In Figure 4c the probability density function is weighted by the number of clouds in, or equivalently mass of, each feature resulting in dense features being more significant. In Figure 4a there is no weighting. In addition, within each graph, there are three curves. The top curve is the calculated probability density function. The middle curve takes into consideration only those features of length greater than 1 kpc, and the bottom curve, those greater than 1.5 kpc. Hence, the bottom curve in Figure 4c supplies the most information concerning the longer, denser, and consequently most prominent features.

Figure 4 exhibits two preferred pitch-angle values. The omnipresent broad peak lying roughly between 20° and 35° can be attributed to segments of the global arms. The secondary peaks at around 40° and just above 50° can be attributed to spurs, bridges, and feathers. There is a rather surprising absence of pitch-angle values both below 15° and above 60°. This is even more astonishing since the underlying density wave modal spiral varies around 10°. The global arms are disjointed; most global arm segments seem to be pulled inward resulting in an increased pitch angle. This may be due to

reverse shear or possibly SSPSF in the global arm causing shells and the formation of highly self-gravitating giant molecular complexes or superclouds which in due course get elongated by differential rotation of the disk. These competing physical mechanisms will be analyzed in a later paper. Note that the density of the secondary features varies independently with position. It can be argued that the denser superclouds are strongly self-gravitating and have extensive internal random motions. These clouds are associated with values of the nondimensional parameter $P/G\sigma_c^2 \ll 1$ (Elmegreen 1991a, b) and are furthermore, predominantly molecular clouds. Here, P is the external pressure, σ_c is the average mass column density of the cloud, and G is the gravitational constant. Self-gravity tends to be more important in regions with relatively large gas densities such as spiral arms. The sparser clouds are more likely diffuse with $P/G\sigma_c^2 \gg 1$ and can accordingly be interpreted as predominantly atomic.

To examine whether or not there is any biasing by the d_{tol} clumping algorithm the a_{tol} algorithm is employed on the same galaxy, and, after application of least squares on both sets of features, the resulting distributions of pitch angle are compared.

For the area tolerance expression given in equation (56), the a_{tol} algorithm is applied to the same distribution of gas clouds in our model galaxy seen in Figure 2. The spiral loci, resulting from application of the same least-squares procedure, are shown in Figure 5. Generally, the same features have been isolated, and the pitch angles seem to be approximately the same. There is, however, one fairly noticeable difference. The spiral loci in Figure 3 are consistently longer than their counterparts in Figure 5. This is because the d_{tol} algorithm includes slightly more clouds in a given feature. Due to the nature of the d_{tol} algorithm, a cloud on the outer edge of a feature is usually considered as contributing to that feature since it is frequently a neighbor of another cloud already satisfying the criterion requiring a "sufficient" number of
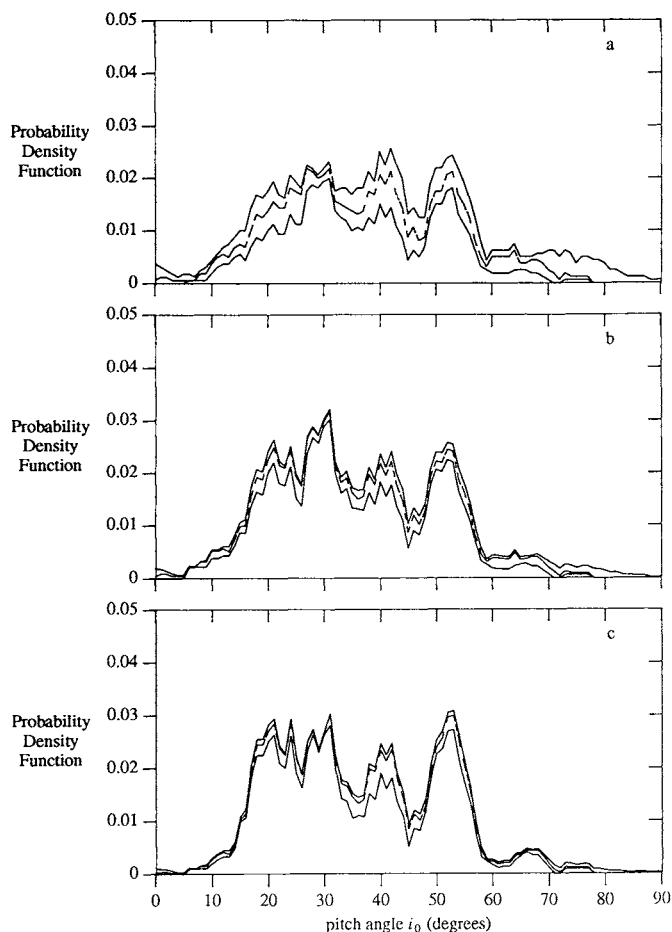

FIG. 4.—Probability density function of pitch angles (a) weighted by length (b) and weighted by mass (c) for model galaxy Case 15 for the spiral loci plotted in Fig. 3. The top curve in each plot is the exact probability density function: the middle and bottom curves represent features longer than 1 and 1.5 kpc, respectively. The bottom curve therefore represents the preferred pitch angles of the most prominent features.
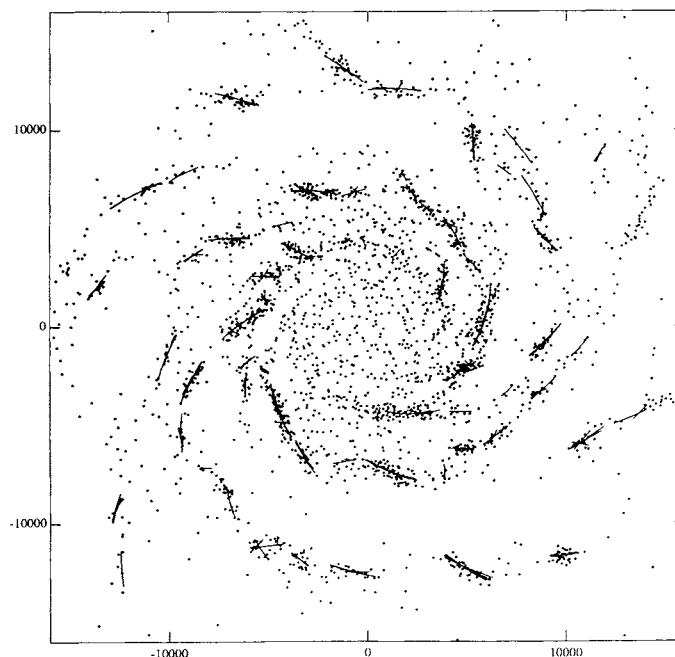

FIG. 5.—Spiral loci for model galaxy Case 15 (Roberts et al. 1992) after employing the a_{tol} partitioning algorithm and the superior fit spiral least-squares method.

clouds within a certain distance. For the a_{tol} algorithm, the same cloud (on the outer edge) will most likely have a fairly large Voronoi area. It will, thus, have been eliminated by this algorithm since large Voronoi areas are associated with sparse regions of the galaxy.

A comparison of Figures 4 and 6 suggests that the added length from employment of the d_{tol} algorithm does not significantly affect the pitch-angle distribution. The distributions, although not exactly the same, do display similar characteristics. In the distributions weighted by mass, that is, the bottom graphs, the bottom curve illustrates that for features greater than 1.5 kpc there are essentially two primary peaks. The broad primary peak between 20° and 35° is attributed to segments of the global arms. The apex at just above 50° is due to spurs and feathers. Considering that features have been isolated using completely different computational methods, it is reassuring to see that the two most important distributions just discussed resemble one another so closely.

The two partitioning algorithms previously employed were applied in Cartesian coordinates. In an effort to determine whether or not the coordinate system employed biased the way in which the features were captured, the a_{tol} analysis was also implemented in $(\ln r, \theta)$ coordinates. In this coordinate system the spiral loci become linear loci. Also, the mean distance between clouds becomes more uniform, and so the a_{tol} partitioning algorithm can be applied with a constant expression

for a_{tol} in equation (9). Using a linear version of the superior fit least-squares method, the resulting distributions of pitch angles were remarkably similar to those presented in Figures 4 and 6 (see Russell 1991).

It can be concluded that the distributions of pitch angles resulting from the application of the a_{tol} and d_{tol} algorithms, along with the superior fit spiral least-squares method, are a direct result of the nature of the galactic distribution of gas clouds and not a result of biasing by the partitioning algorithms, nor the coordinate system in which they are implemented. The distributions are not skewed by the numerical methods, but depend upon the morphology of the galaxy under investigation.

5. CONCLUSIONS

The primary goal of this research was to develop an automated mathematical method which could successfully isolate the many different features in prototype and observed spiral galaxies and accurately measure the pitch angles and lengths of these individual features. This was achieved by an effective synergism of the properties of the Voronoi diagram and a modified spiral least-squares algorithm. The method was applied to analyze the evolution of specific features in a prototype galaxy exhibiting flocculent spiral structure.

The mathematical-computational method was separated into two components. Initially, the galaxy was partitioned into dense regions constituting features using two different methods. The results obtained using these two partitioning algorithms were very similar, implying that no numerical biasing was evident and that capturing of the features was consistent.

After the clouds composing each feature were ascertained, various least-squares methods were employed to calculate the preferred orientation of the cloud distributions. In the development and analysis of the least-squares methods it was determined that standard least-squares methods underestimated the true slope of the distribution and, furthermore, were incapable of approximating an orientation of 45°. By introducing a superior fit least-squares method, developed with the intention of calculating true orientation rather than a regression line, the problems were overcome. Since most of the features formed were of spiral shape due to differential rotation, a $(\ln r, \theta)$ coordinate system was employed to perform the least-squares analysis. The features of a simple test galaxy were successfully separated and their pitch angles approximated accurately.

The model galaxy which combined 10%–15% spiral forcing with 6% gas mass fraction exhibited local and mesoscale features with preferred pitch angles between 20° and 40° attributed primarily to prominent segments, spurs, feathers, and secondary features of the global arms. The secondary peak at 50° was attributed to prominent spurs protruding from the outer edge of the global arms at large radial values. These results corroborate observational data obtained by Elmegreen (1980) and Weaver (1970). Further corroborating results are found by Russell & Roberts (1992) who extend the numerical methods and algorithms developed in the present paper for application to two observed galaxies, M101 and NGC 1232.
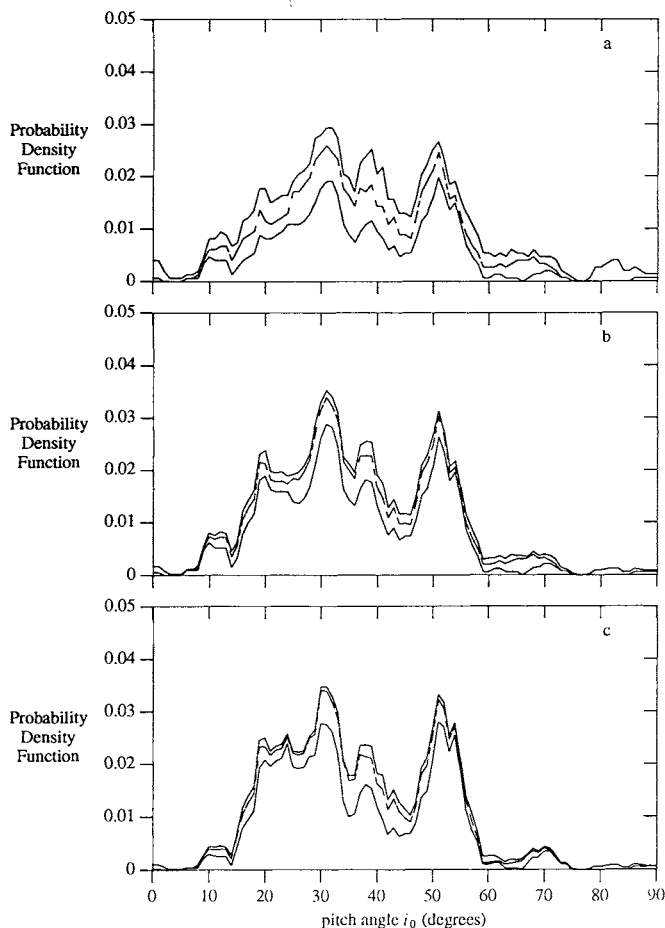
FIG. 6.—Probability density function of pitch angles (a) weighted by length (b) and weighted by mass (c) for model galaxy Case 15 associated with the spiral loci in Fig. 5.

APPENDIX

TESTING THE NUMERICAL METHOD

Each compartment of the overall numerical method is tested on a simple test galaxy for which the features and their primary characteristics are known. The test galaxy seen in Figure 7 is generated by using portions of spiral arms inclined at constant pitch angles. To verify that the algorithm splits up features successfully, the portions of the spiral arms in the test case are all distinct. To demonstrate that the least-squares algorithm is able to capture more than one prominent pitch angle, two different i_0 values are introduced. Features at 10° are of different length and density than those at 45°; this difference should be portrayed in the resulting probability density functions. Since the global spiral arms in the model galaxies of Roberts et al. (1990, 1992) closely approximate 10°, it is the inclination chosen for the longer spiral segments; 45° was chosen to portray the inadequacy of the standard least-squares method in successfully approximating this value.

The properties of a spiral feature are of course nonlinear, but for short features the spiral shape is difficult to distinguish. Hence, a linear estimate is often sufficient. Various linear least-squares methods were applied to the test galaxy as well as various prototype galaxies of Roberts et al. (1992) (see also Russell 1991). In general, the linear methods successfully modeled the shorter features, but for galaxies exhibiting long arm branchings, linear methods were found to be inaccurate.

For model galaxy simulations where the amount of self-gravitational forcing is kept to a minimum, the long global spiral arms become more prominent. Since the longer global arms asymptotically approach logarithmic spirals, the search for features of this shape was initiated. Various spiral least-squares methods are applied to the test galaxy.

Following the derivation in § 3 for the standard spiral least-squares method, least-squares regression lines of the forms $\theta = \hat{\alpha} + \hat{\beta} \ln r$ and $\ln \hat{r} = \hat{\gamma} + \hat{\delta}\theta$ are estimated for each feature. The estimate which produces the least absolute error is taken as the best approximation to the orientation of the cloud distribution constituting a given feature. The spiral loci representing each of these estimates associated with each feature are seen in Figure 7.

It is clear that all distinct features are isolated successfully by the a_{tol} algorithm, and their orientations are modeled adequately by the standard spiral least-squares method. The accuracy of the loci is also seen to be independent of the length of the features.

Seen in Figure 8 is the probability density function (weighted by feature mass) associated with the set of regression lines in Figure 7. The 10° peak is produced as expected, but the other expected peak is bisected at 45°. The value of zero at 45° implies that no features were modeled with pitch angles between 42°.5 and 47°.5. Standard spiral least squares calculates two regression lines.
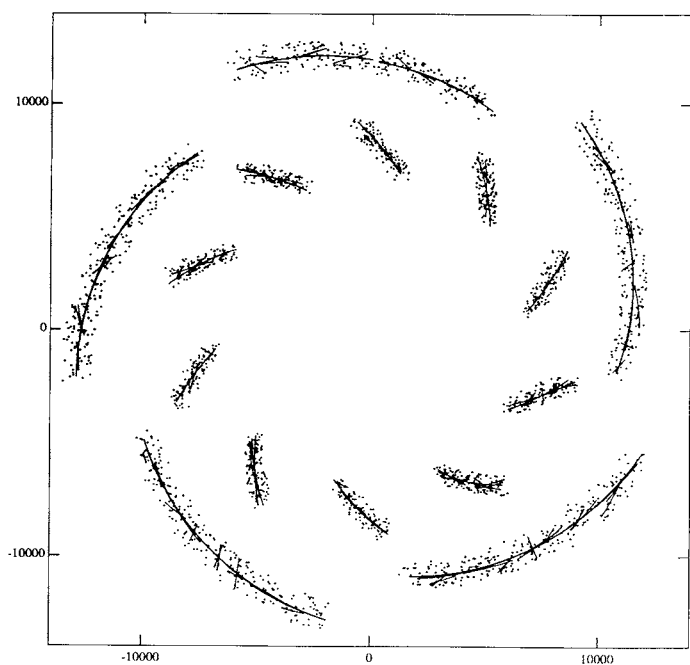

FIG. 7
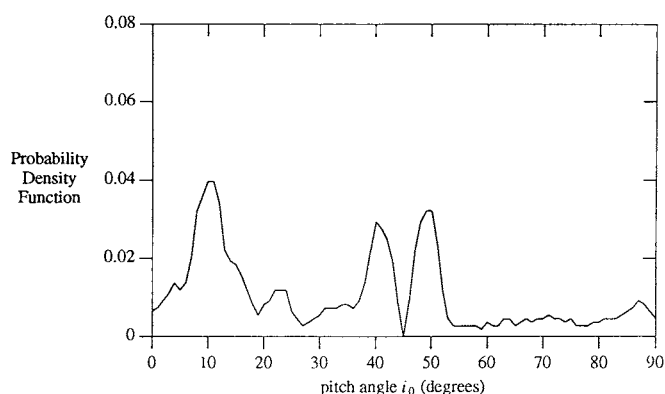

FIG. 8

FIG. 7.—Test galaxy exhibits 10 features at constant pitch angles of 45° between 7 and 9 kpc, and five features at 10° between 11 and 13 kpc all evenly spaced axially around the galaxy. For each of the 45° features, 250 particles are distributed initially along each arm. The (x_i, y_i) positions are randomly perturbed up to 5% of the radial value. The 10° arms have 500 particles, each perturbed in the same fashion. None of the spiral segments overlap; each feature formed by either of the partitioning algorithms has one preferred pitch angle and is unaffected by stray particles from another neighboring feature. The spiral loci produced, after employing the a_{tol} partitioning algorithm and the standard spiral least-squares method, are included. The loci closely approximate both the orientation and length of each distinct feature.

FIG. 8.—Probability density function of pitch angles weighted by mass associated with the spiral loci seen in the test galaxy in Fig. 7 produced by the a_{tol} partitioning algorithm and the standard spiral least-squares method. The 10° pitch angle is captured, but the 45° orientation has been either underestimated or overestimated for each regression spiral resulting in a separation of the peak.
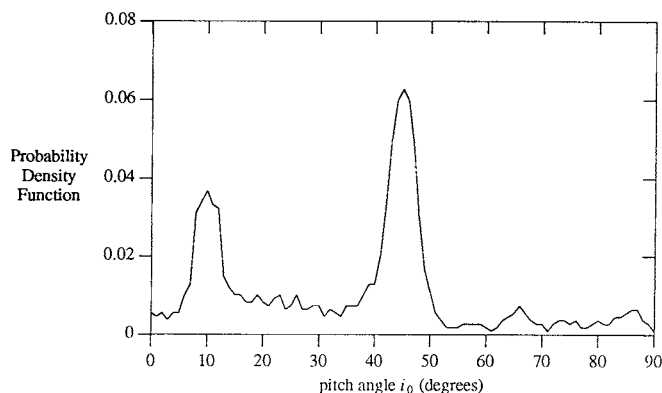
FIG. 9.—Probability density function of pitch angles weighted by mass associated with the spiral loci produced using the a_{tol} partitioning algorithm and the superior fit spiral least-squares method. The 45° peak is now modeled accurately since the superior fit least-squares algorithm fits a unique best-fit spiral locus.

The $\hat{\theta} = \hat{\alpha} + \hat{\beta}\ln r$ estimate has produced values of $i_0 < 45°$, and the $\ln\hat{r} = \hat{\gamma} + \hat{\delta}\theta$ estimate has produced values of $i_0 > 45°$. In general, standard least squares tends to produce a regression line with slope less than that of the true orientation of the data. Hence, depending on the regression line chosen in the standard least-squares method, the orientation is pulled either side of the true value of 45°.

The superior least-squares method overcomes this problem. The resulting spiral loci are almost exactly the same as those seen in Figure 7, but the associated probability density function presented in Figure 9 shows the expected peak at 10° and 45°. Again, this distribution is weighted by the mass of each feature, and since the majority of the features are inclined at 45° the associated peak is more prominent than that at 10°.

REFERENCES

Abramowitz, M., & Stegun, I. E. 1972, Handbook of Mathematical Functions (New York: Dover)
Adler, D. S. 1989, Ph.D. thesis, Univ. Virginia
Bertin, G., Lin, C. C., Lowe, S. A., & Thurstans, R. P. 1989a, ApJ, 338, 78
———. 1989b, ApJ, 338, 104
Blum, H. 1973, J. Theoret. Biol., 38, 205
Brostow, W., Dussault, J.-P., & Fox, B. L. 1978, J. Comput. Phys., 29, 81
Carlberg, R. G., & Freedman, W. L. 1985, ApJ, 298, 486
Dirichlet, G. L. 1850, Z. Reine Angew. Math., 40, 216
Elmegreen, B. G. 1991a, in Physics of Star Formation and Early Stellar Evolution, ed. N. Kylafis & C. J. Lada (Dordrecht: Kluwer), 35
———. 1991b, in Protostars and Planets III, ed. E. H. Levy & M. S. Matthews (Tucson: Univ. Arizona Press), in press
Elmegreen, D. M. 1979, ApJS, 43, 37
———. 1980, ApJ, 242, 528
Gerola, H., & Seiden, P. E. 1979, ApJ, 223, 129
Hausman, M. A., & Roberts, W. W. 1984, ApJ, 282, 106
Kiang, T. 1966, Z. Ap., 64, 433
Levinson, F. H., & Roberts, W. W. 1981, ApJ, 245, 465
Lin, C. C., & Shu, F. H. 1964, ApJ, 140, 646
———. 1966, Proc. Natl. Acad. Sci., 55, 229
Lowe, S. A. 1988, Ph.D. thesis, MIT
Lynds, B. T. 1970, in IAU Symp. 38, The Spiral Structure of Our Galaxy, ed. W. Becker & G. Contopoulus (Dordrecht: Reidel), 26
Miller, R. H. 1976, J. Comput. Phys., 21, 400
———. 1978, ApJ, 223, 811

Miller, R. H., & Smith, B. F. 1979a, ApJ, 227, 407
———. 1979b, ApJ, 227, 785
Mueller, M. W., & Arnett, W. D. 1976, ApJ, 210, 670
Rhynsburger, D. 1972, Masters thesis, Univ. Michigan
———. 1973, Geogr. Anal., 5, 133
Roberts, W. W. 1992a, in Reference Encyclopedia of Astronomy and Astrophysics, ed. S. P. Maran (New York: Van Nostrand Reinhold), 218
———. 1992b, in Ann. NY Acad. Sci., Astrophysical Disks, ed. S. F. Dermott, J. H. Hunter, & R. E. Wilson, 675, 93
———. 1993, PASP, in press
Roberts, W. W., & Adler, D. S. 1989, in Applications of Computer Technology to Dynamical Astronomy, ed. P. K. Seidelmann & J. Kovalevsky (Dordrecht: Kluwer), 285
Roberts, W. W., Adler, D. S., Lowe, S. A., & Lin, C. C. 1992, ApJ submitted
Roberts, W. W., & Hausman, M. A. 1984, ApJ, 277, 744
Roberts, W. W., Lowe, S. A., & Adler, D. S. 1990, in Ann. NY Acad. Sci. 596, Galactic Models, ed. J. R. Buchler, S. T. Gottesman, & J. H. Hunter, Jr., 130
Roberts, W. W., & Stewart, G. R. 1987, ApJ, 314, 10
Russell, W. S. 1991, Ph.D. thesis, Univ. Virginia
Russell, W. S., & Roberts, W. W. 1992, ApJ, 398, 94
Seiden, P. E., & Gerola, H. 1979, ApJ, 233, 56
Smith, B. F., & Miller, R. H. 1986, ApJ, 309, 522
Stephens, M. A. 1974, J. Am. Stat. Assoc., 69, 730
Voronoi, G. 1908, J. Reine Angew. Math., 134, 198
Weaver, H. F. 1970, IAU Symp. 39, Interstellar Gas Dynamics, ed. H. Habing (Dordrecht: Reidel), 22